Modeling of the pellet cloud evolution and mass deposition with account of ∇B induced drift

I.Yu. Senichenkov [a], I.Yu. Veselova[a], V.A. Rozhansky[a], R. Schneider[b]

[a]*St-Petersburg State Polytechnical University, 195251, St-Petersburg, Russia*

[b]*Max-Planck-Institut für Plasmaphysik, Teilinstitut Greifswald, Euratom Association, D-17491, Greifswald, Germany*

Abstract

Modeling of the pellet ablation cloud evolution including the ∇B induced drift motion is performed. The model includes cloud heating, expansion and ionization, acceleration in the low-field-side direction, Alfven conductivity of the background plasma, compensation of ∇B currents in different parts of the cloud during its propagation along the magnetic field, cooling of the background plasma and simulation of the pellet ablation rate in a self-consistent manner. The time evolution of cloud density and temperature profiles and the mass deposition after the pellet injection are calculated. The low field side and high field side injection scenarios with plasma and pellet parameters typical for ASDEX-Upgrade tokamak are compared. An effect of pre-cooling on the pellet penetration depth is studied. The calculated size of the neutral part of the cloud, the characteristic values of cloud density and temperature far from the pellet and the fuelling efficiency (for LFS pellets) are in reasonable agreement with those observed in experiments on ASDEX-Upgrade.

Keyword: Ablation, Fuelling efficiency, Pellet, Drift

PACS numbers: 52.65.Kj, 52.25.Fi

***Corresponding Author Address:** 195251, St.-Petersburg State Polytechnical University, Physical Technical Faculty, Polytechnicheskaya, 29, St-Petersburg, Russia

***Corresponding Author e-mail:** senichenkov@edu.ioffe.ru

Introduction

Pellet injection is considered as the most promising way of refueling for future tokamaks and stellarators. The density rise and temperature decrease after the pellet injection affects both fusion power and confinement regime. The density and temperature profiles are defined by the motion of the pellet ablation cloud and heat balance inside it.

The pellet injected into the plasma evaporates rapidly producing a neutral gas around it, which moves together with the pellet with its velocity V_p. The neutral cloud expands mainly spherically, while after the ionization it propagates mainly along the magnetic field lines and drifts towards the low field side (LFS) direction in the crossed electric and magnetic fields. The formation of this electric field is determined by the following factors: plasma acceleration in the LFS direction, Alfven conductivity of the background plasma and compensation of the ∇B currents in different parts of the cloud propagating along the magnetic field [1]. As it is shown in [1-4], this $\vec{E} \times \vec{B}$ drift is responsible for significant displacement of the ablated material from the magnetic surfaces where the ablation took place towards LFS. This displacement takes place on a time scale of hundreds microseconds, which is of the same order as the pellet lifetime. This effect leads to a higher fueling efficiency (which is defined as a ratio of total plasma electrons rise after the pellet injection to the number of atoms in the pellet) for high field side (HFS) injection in comparison with the injection from the LFS. This effect was predicted in [5,6] and was observed by P. Lang et al. [7] on the ASDEX-Upgrade, Baylor et al on DIII-D [4] and confirmed for other tokamaks [8,9].

The electric field inside the pellet cloud and its drift velocity are defined by cloud density, temperature and ionization degree. Therefore, to predict the density shift after pellet injection one has to simulate the cloud evolution self-consistently.

Up to now, a full simulation of cloud pattern with account of the $\vec{E} \times \vec{B}$ drifts was absent. First results of such a simulation obtained by means of LLPD code for the LFS pellet injection were presented in [10]. In the present paper, the LLPD code is improved so that also the modeling of the HFS pellet injection becomes possible. This code is a modification of the LLP code [11], which originally was used for the simulation of pellet ablation in a tokamak. The main feature of the new LLPD code is that the drift effects are taken into account. Thus, the model includes cloud heating, expansion and ionization, acceleration in the low-field-side direction, Alfven conductivity of the background plasma, compensation of ∇B currents in different parts of the cloud during its propagation along the magnetic field, cooling of the background plasma (including a pre-cooling of central magnetic surfaces before the pellet by drifting materials in the case of HFS pellet injection) and simulation of the pellet ablation rate in a self-consistent manner. By means of the LLPD code one can calculate the evolution of all cloud parameters, its drift velocity, the final material displacement, the fueling efficiency and final background plasma density and temperature profiles after the pellet injection.

Recently, a theoretical model for the drift motion of ablated material together with its longitudinal expansion was proposed by Parks [3]. In that model (similarly to [2]) assumed is the periodical separation of 'detached cloudlet' from the pellet cloud, and the drift of the cloudlet is considered. The main mechanisms of polarization formation and reducing are suggested to be, besides considered in this paper, the inertial force caused by cloud expansion along curved filed lines, pressure equilibration and a shear of magnetic field.

Below results of pellet cloud evolution simulations by the LLPD code both for HFS and LFS pellets are presented. The pellet cloud parameters and the fuelling efficiency computed by the new LLPD

code are in a qualitative agreement with those measured on ASDEX-Upgrade by Lang et al [7] and Müller et al [12]. The obtained results might be used for the optimization of the pellet injection schemes in future experiments.

The paper is organized as follows. In the next section the model used in the LLPD code is described. Afterwards, the code LLPD itself is briefly described, and finally the simulation results are presented and compared with experiments.

Physical model

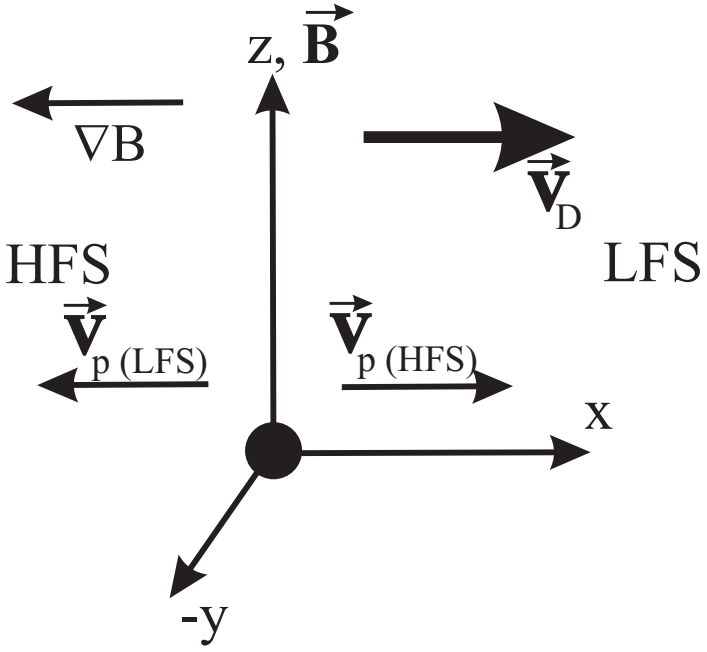

Figure 1. The geomery considered in the model. Shown are the ∇B direction, the direction of drift and the two considered pellet velocity directions.

The model takes into account pellet ablation, neutral and ionized gas expansion, ionization, magnetic confinement, collision energy transfer, radiation losses, cooling of the ambient plasma and a ∇B -induced polarization electric field. The presence of a self-generated electrostatic field in the cloud and the electrostatic sheath at the cold cloud – hot plasma interface is also taken into account. The particle and energy flux depletion of hot background particles in the shielding cloud due to collision interaction with the cold particles is determined by the stopping length calculations applied to both electron and ions. The model includes calculation of the energy transport (both convective and conductive) in the direction normal to the magnetic field for a given set of background plasma and pellet parameters and a magnetic flux surface topology.

As it is already mentioned, the code LLPD is a modification of the LLP code, which is described in [11]. A slab geometry is considered, the magnetic field is directed along the z-axis, the x-axis is directed opposite to the direction of ∇B , see Fig. 1. The effects of magnetic filed lines curvature and the finite tokamak volume (the finite energy contents of the ambient plasma) are taken into account in the equations for the polarization electric field and ambient plasma cooling as described below.The following set of single fluid MHD equations is solved

$$\frac{\partial \rho}{\partial t} + \left(\nabla \cdot \left(\rho \vec{V}\right)\right) = S, \tag{1}$$

$$\frac{\partial}{\partial t}\left(\rho \vec{V}\right) + \left(\nabla \cdot \left(\rho \vec{V}\right)\vec{V}\right) = -\nabla p + \left[\vec{j} \times \vec{B}\right], \tag{2}$$

$$\frac{3}{2}\frac{\partial p}{\partial t} + \frac{3}{2}\left(\nabla \cdot p\vec{V}\right) = -\left(\nabla_{\parallel} \cdot \mathbf{q}_{inc}\right) + \left(\nabla \cdot \chi \nabla T\right) - p\left(\nabla \cdot \vec{V}\right) - Q_{ioniz} - Q_{rad\_losses} + \frac{j^2}{\sigma} \tag{3}$$

Here $\rho = Mn_h$ is the mass density, M is the mass of pellet atoms, n_i, $i = 0..Z$ is the density of ions in the charge state i, $n_h = \sum_{i=0}^{Z} n_i$ is total atoms and ions density, $\vec{V}$ is the expansion velocity, S is a particle source representing a pellet, $p = (n_e + n_h)T$ is the total pressure, $n_e = \sum_{i=0}^{Z} i \cdot n_i$ is the electrons density, $\vec{j}$ is the current density, $\vec{B}$ is the magnetic field, T is a temperature common for all species, q_{inc} is the energy flux carried by the incident electrons and ions from the ambient plasma, χ is the heat conduction coefficient, Q_{ioniz} and Q_{rad_losses} are the ionization and radiation loss power per volume respectively, $\sigma = \frac{n_e e^2}{m_e(\nu_{ea} + \nu_{ei})}$ is the local electric conductivity calculated with account of electron-neutral and electron-ion collisions.

The ionization state distribution is described by

$$\frac{dy_i}{dt} = n_e\left(y_{i+1}R_{i+1} - y_i(I_i + R_i) + y_{i-1}I_{i-1}\right) + n_e^{(inc)}\left(y_{i-1}I_{i-1}^{(inc)} - y_i I_i^{(inc)}\right),\ i = 0 \div Z \qquad (4)$$

where $y_i = n_i / n_h$, I_i and R_i are the ionization and recombination rates respectively, $y_{-1} = y_{Z+1} = 0$, $R_0 = I_Z = 0$, $\frac{d}{dt} = \frac{\partial}{\partial t} + (\vec{V} \cdot \nabla)$. For the dense deuterium pellet cloud, the Local Thermal Equilibrium rates [13] are used in the first term of the r.h.s. of (4). The second term in the r.h.s. represents ionization by incident electron impact, the ionization rates are published in [14].

The electrostatic shielding potential is calculated according to ambipolarity and quasi-neutrality conditions [15] including possible incident particle fluxes penetrating throughout the cloud. The longitudinal (along B) electric field inside the cloud is calculated from the ambipolarity condition

$$j_{\parallel} = e(\Gamma_{ih} - \Gamma_{eh}) + \sigma E_{\parallel} - \sigma \frac{T}{e}\left(g_T \frac{\partial}{\partial z}\ln T + \frac{\partial}{\partial z}\ln n_e\right) = 0 \qquad (5)$$

where Γ_{eh} and Γ_{ih} are the incident electrons and ions fluxes respectively.

The depletion of incident electrons and ions is calculated exactly as it is done in the LLP code [11] by representing the Maxwellian distribution through multiple mono-energetic groups [16].

The drift velocity $\vec{V}_D$ towards LFS and the corresponding polarization electric field $\vec{E}_{pol} = [\vec{B} \times \vec{V}_D]$ are defined by the following current balance equation integrated along the magnetic field lines [1]

$$\frac{M}{B^2}\int_{-\infty}^{+\infty} n_h dz \frac{d\vec{E}_{pol}}{dt} = -2\Sigma_A \vec{E}_{pol} + \frac{\tilde{\alpha}(L_c)}{B^3}\int_{-\infty}^{+\infty}(n_e + n_i)Tdz[\nabla B \times \vec{B}] \qquad (6)$$

In the slab geometry used in the code $\left|\frac{[\nabla B \times \vec{B}]}{B^3}\right| = \frac{2}{BR}$, where R without subscript denotes the major radius (while R_i with subscript is the recombination rate). The term in the l.h.s. is the polarization current, the first term in the r.h.s. is the total vertical current in the ambient plasma caused by Alfven

wave propagating along the magnetic field lines, and the last term in the r.h.s. is the ∇B-induced current (the factor 2 is due to the magnetic field lines curvature). Here $\Sigma_A = \frac{1}{B}\sqrt{\frac{m_0 n_0}{\mu_0}}$ is so-called Alfven conductivity, n_0 and m_0 are the density and the ion mass of the ambient plasma, L_c is the characteristic cloud length along the magnetic field defined as $L_c = \frac{\int_{-\infty}^{+\infty} p dz}{p_{\max}}$ and a function $0 \le \tilde{\alpha}(L_c) \le 1$ is introduced to model how the ∇B induced current inside the cloud vanishes while the cloud expands along B.

This function $\tilde{\alpha}(L_c)$ represents the effect that after a poloidal turn at π radians due to the expansion along $\vec{B}$, the ∇B induced current inside the cloud reduces significantly (see details in [1]). Since the ∇B induced current decay time is smaller than the pressure equilibration time, the pressure equilibration should not play a significant role in the cloud stopping. To define the exact behavior of the function $\tilde{\alpha}(L_c)$ one should solve a full 3D problem of potential formation and currents flow. At least, to study the effect of ∇B-induced current cancellation it is necessary to consider the problem without integration along the magnetic field. Consequently, the function $\tilde{\alpha}(L_c)$ cannot be calculated in a frame of considered approach and is an external parameter to the model. Since up to now such a problem is not yet solved, one can only introduce some approximation of $\tilde{\alpha}(L_c)$. To do this in the paper we follow the logic of [1]. As the cloud half-length L_c exceeds $\pi q R/2$ (which corresponds to the poloidal extension of whole cloud of π radians), the ∇B induced currents at the symmetrical over $z=0$ most distant from the pellet parts of the cloud becomes closed by longitudinal conductivity currents $j_{\|} = -\sigma_{\|} E_{\|}$. The ∇B induced current fully vanishes as the cloud length exceeds its critical value $L_{c0} = \pi q R$.

In the present model we do not consider a $q(r)$ profile, therefore we use some average value of safety factor q_{avr}. If one chooses $q_{avr} = 2$, then one get $L_{c0} = 2\pi R$. In the present calculations we use

$$\tilde{\alpha}(L_c) = \begin{cases} \cos\left(\frac{\pi L_c}{2 L_{c0}}\right), & L_c < L_{c0}, \\ 0, & L_c \ge L_{c0}. \end{cases}$$

with $L_{c0} = R$. Our calculations (performed below) show that when $L_c = \frac{\int_{-\infty}^{+\infty} p dz}{p_{\max}}$ reaches R, the z-coordinate of last physical Lagrangian cell (the definition of L_c used in [10]) is about $(1-2)\cdot \pi R$.

It is worth mentioning again that the function $\tilde{\alpha}(L_c)$ is an external parameter, which is still to be calculated. As it will be demonstrated below, the calculations with such a rough definition used in this paper can qualitatively reproduce the magnitude of material displacement and drift velocity.

The ambient plasma cooling is described by

$$3 n_0 \frac{dT_0}{dt} = \left(\nabla_{\|} \cdot \mathbf{q}_{inc}\right) \qquad (7)$$

The common temperature of ambient electrons and ions is assumed. Since the density equilibration time $2\pi qR\sqrt{M/T}$ is larger than the pellet lifetime, the ambient electron density is moved outside the time derivative operator. It is assumed that the heat conduction in ambient plasma is almost infinitely large and temperature equilibration over magnetic surface is almost instant. The particle and temperature radial transport is not considered in the present model.

Computational model

The spherical pellet of a given radius r_p is assumed to be injected horizontally in equatorial plane with the velocity V_p, which is assumed to be constant during pellet ablation, towards the center of a tokamak either from HFS or LFS. Only in these cases the cloud expands in two directions – direction of magnetic field $\vec{B}$ (toroidal) and direction of $\vec{V}_p$ (radial), which coincide with the direction of $\vec{V}_D$. In the third direction (poloidal), perpendicular to both $\vec{B}$ and $\vec{V}_p$ the cloud is stopped by the Lorentz force (see [17]), and only slow diffusion is possible. As it was shown by numerical simulation in [1], in the cloud drifting towards the LFS this diffusion compensates the convergence of equipotentials, along which particles drift, and therefore the poloidal cloud size remains almost constant. In the present modeling we set it to its value once calculated in the vicinity of the pellet. Thus the x-coordinate may be treated as the tokamak minor radius.

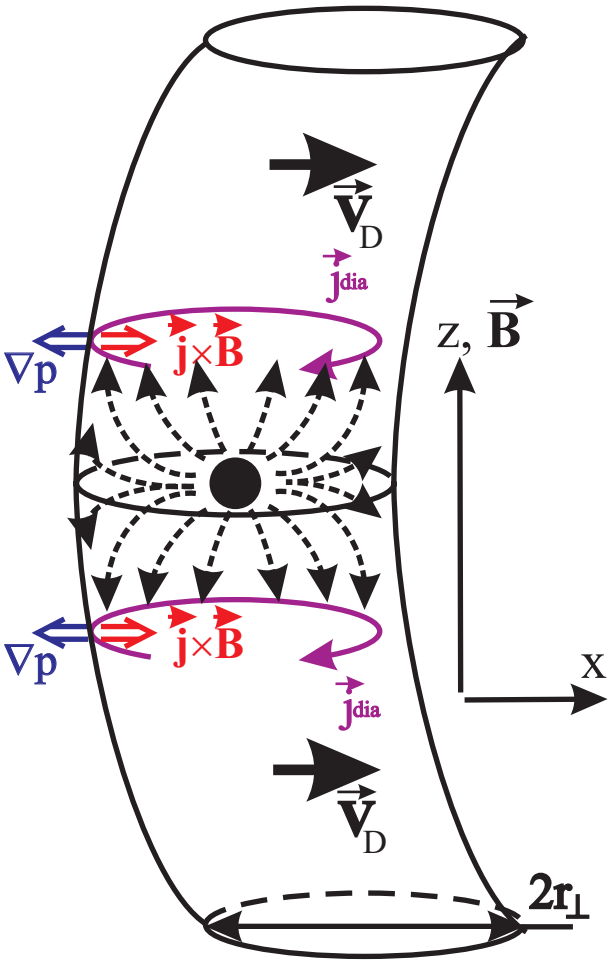

Figure 2. The schematic view of the cloud in the vicinity of the pellet.

The ambient temperature and density profiles before the injection, the tokamak magnetic field and volumes inside the magnetic surfaces are assumed to be known.

The cloud expansion in the vicinity of the pellet is calculated by two major blocks of the LLP code [11], running one after another in iterative manner. The first block calculates for a given particle source strength the expansion across the magnetic field lines and the ionization radius. In this block – the separate B-perpendicular code – the equations (1)-(6) are solved with the help of Lagrangian cells representation. The cloud is discretized in the radial ($B_\perp$) direction, the axial ($B_\parallel$) expansion of each Lagrangian cell also being taken into account without discretization in that direction. The result of this modeling is that particles after the ionization do not freely expand across B, but are confined in a tube with radius $r_\perp$ almost equal to the ionization radius [18,19], see Fig 2. The second block – the separate B-parallel expansion code – calculates the longitudinal (along B) expansion of the particles confined in such a tube.

The equations solved are the same - (1)-(6), but the pellet ablation rate is calculated self-consistently. The Lagrangian cells representation is used, the discretization is done in the direction along the magnetic field. The calculation is performed within the residence time interval $t_{res} = 2r_\perp / V_p$, the calculated ablation rate is used as a particle source strength for the B-perpendicular code at the next iteration.

The drift motion in the B-parallel code is organized by reducing the number of particles in each cell N_l (l is the Lagrangian cell index) according to

$$N_l = N_{beg}\left(1 - \frac{\Delta R_l}{2r_\perp}\right)$$

where $\Delta R_l = \int^t V_D d\tau$, N_{beg} is the initial number of particles in the cell, the same for each cell, and the drift velocity V_D is defined by (6). Thus, the cloud shape and cloud parameters profiles (density, temperature, ionization degree) in the vicinity of the pellet are quasi-stationary. The ablated particles expand mainly spherically being neutral, after ionization they expand mainly along the magnetic field, then, as their temperature increases, they accelerate towards the LFS, see Fig 2. The characterizing cloud length along the magnetic field may be estimated as $\sqrt{r_\perp R}$ [5].

The pellet motion is modeled by changing the values of the ambient plasma density and temperature in time. After one residence time, the new confinement radius and the ablation rate are calculated in the iterative procedure described above for the ambient plasma density and temperature corresponding to the new pellet position $x_i = x_{i-1} \pm (r_{\perp i} + r_{\perp i-1})$ (the sign $\pm$ corresponds to the HFS or LFS pellet).

The particles removed from the tube containing the pellet form a pellet 'wake' behind (for the LFS pellet) or before (for the HFS pellet) the pellet, which is stretched from the current pellet position up to the separatrix. The expansion of these particles along the magnetic field is modeled by the B-parallel code with the ablation rate set to zero. To do this, the pellet wake is discretized in x direction to several tubes with radius $r_{\perp i}$. The particles move from one tube to another due to the drift, the drift particle, momentum and energy fluxes are calculated according to Eq. (6).

In the vicinity of the pellet, where the cloud is dense and Alfven conductivity current is negligible, the ionized particles accelerate with acceleration $g = \frac{4T}{MR}$ up to the velocity $V_\infty = \frac{2}{BR\Sigma_A}\int_{-\infty}^{+\infty} T(n_e + n_i)dz$. This value comes from equating two terms in the r.h.s. of Eq. (6). As the cloud expands along the magnetic field, the acceleration term (the last one in the r.h.s) vanishes, and the drift velocity decreases to zero.

If the drift velocity reaches zero inside the separatrix, the particles are treated as deposited at the magnetic surface where they are stopped, and the temperature at this surface is reduced adiabatically. Again the instant temperature equilibration is assumed, but the ambient plasma density is not changed. Instead, the number of particles deposited at each magnetic surface is counted, and only after all particles are deposited, the density rise is calculated as a ratio of number of particles, deposited at each surface, to the volume between surfaces.

If the particles cross the separatrix, they are treated as lost. The presence of these lost particles makes the fueling efficiency less than unity. The calculations stop when the pellet fully evaporates and all the ablated particles become either deposited or lost.

This approach allows to determine the pellet cloud parameters in the pellet vicinity and far away in the pellet wake together with the ambient plasma temperature profile at any time moment during the pellet evaporation. During this, the mass deposition and the cooling of ambient plasma are calculated.

Results of the simulations

Ablation rate and pre-cooling effect

Calculations were done for the plasma and pellet parameters corresponding to a typical ASDEX-Upgrade scenario, ($B = 2.5\,\mathrm{T}$, central temperature and density are $n_0 = 3.7 \cdot 10^{19}\ \mathrm{m}^{-3}$, $T_0 = 3.6\,\mathrm{keV}$, last close surface position is at r=41.96 cm.) The pellet characteristics are r_p = 1.2 mm, $V_p = 560\,\mathrm{m/s}$. For the modeling of the HFS pellet, the ambient plasma temperature and density profiles were symmetrized, as it is shown in Fig 3. This was done to simplify the comparison of the HFS and LFS pellets, effects of non-symmetric magnetic surfaces (Shafranov shift) are intentionally ignored.

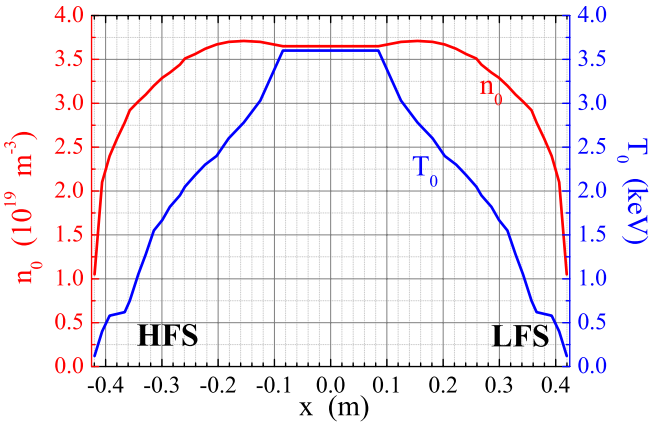

Figure 3. Ambient plasma density and temperature profiles used in the simulations.

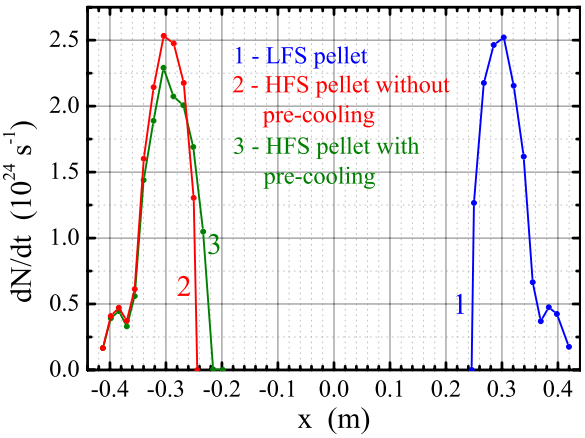

Figure 4. The calculated ablation rate.

The calculated ablation rates for the HFS and LFS pellets are presented in Fig. 4. The ablation rate (for the LFS pellet) and the corresponding penetration depth obtained by means of the new code correspond to the predictions of NGPS scaling [20]. For the HFS pellet, the ablation curve calculated is also shown when pre-cooling of the ambient plasma is turned off, which, naturally, coincide with the ablation curve for the LFS pellet. One can see that the pre-cooling reduces the ablation rate, but the difference is not significant. Therefore one may conclude that the effect of cooling of the plasma in front of the pellet by drifting material on the ablation rate is weak. However, this result depends on pellet and plasma parameters. To see it we reduced the temperature two times and kept other parameters not changed. The calculated penetration depth for the LFS pellet raised up to 36 cm, while for the HFS pellet it exceeds 80 cm. This significant difference may be explained in a following way. For the scenario with higher temperature the penetration depth (20 cm) is smaller than the shift distance of ablated material $\Delta x \approx 40$ cm, and the latter is about the minor radius (41.96 cm.). Therefore the most particles are

deposited in the center, which is cooled significantly (see Figures 5 and 6), because the energy content there is small and perturbation by drifting material is significant. In the same time pellet evaporates within almost unperturbed peripheral region, and almost does not feel the pre-cooling. For the scenario with lower temperature the drifting material again cools the central region, but (due to lower temperature) pellet does not have time to evaporate before it reaches cooled surfaces. Therefore pellet ablation there took place with the very low ambient plasma temperature, and pellet penetration depth increases.

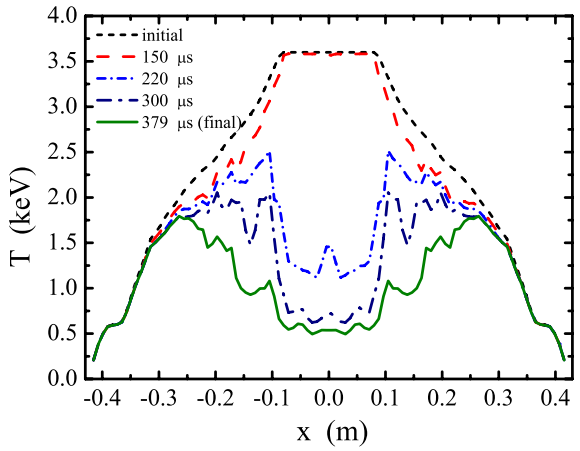

Figure 5. Background temperature evolution after HFS pellet injection. Moment t=0 corresponds to a start of pellet ablation.

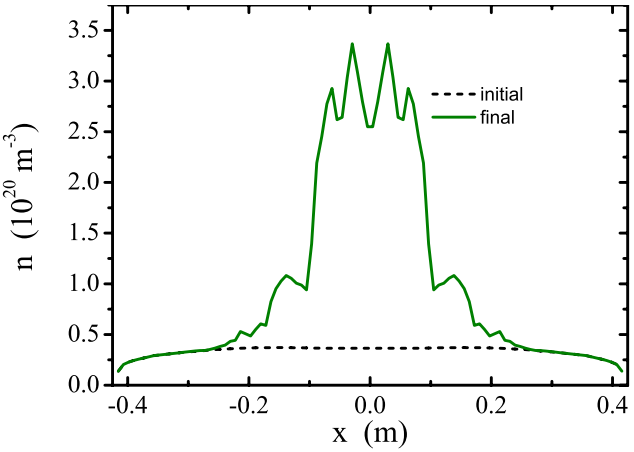

Figure 6. Density rise after pellet injection after HFS pellet injection.

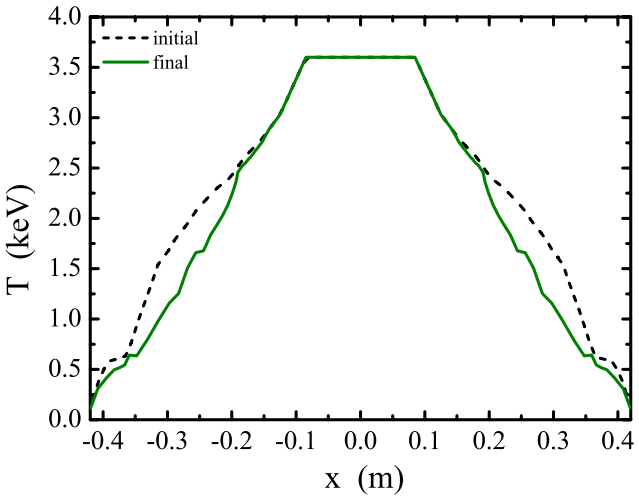

Figure 7. Background temperature decrease after LFS pellet injection.

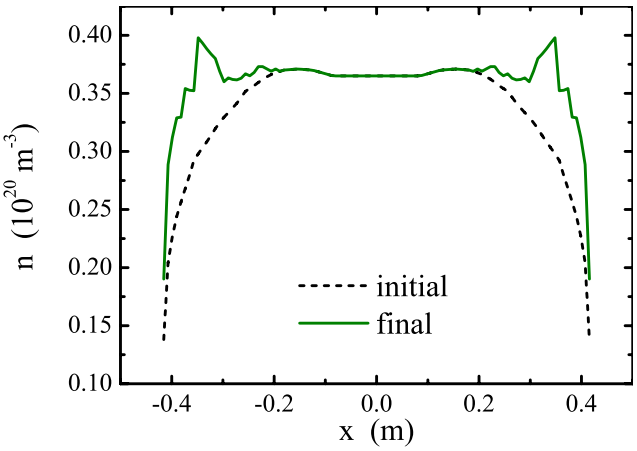

Figure 8. Density rise after pellet injection after LFS pellet injection.

The temperature decrease and density rise caused by the LFS pellet (high temperature scenario) are presented in Figures 7 and 8. One can see again that ablated material does not reduce the ambient plasma temperature significantly at the plasma periphery.

Note that in the analysis performed above important is that the drifting material crosses the tokamak center, which is a geometry effect. For the vertical injection, as it shown in Figure 9, the drifting material does not reach the tokamak center (if pellet penetration depth is smaller than minor radius), and density peak and temperature hollow shown in Figures 5 and 6 cannot appear. Correspondingly, for such pellets the pre-cooling should be weak.

This consideration may explain why did the code LLP without account of drift and pre-cooling [11] reproduce the pellet penetration depths on ASDEX-Upgrade for different injection angles [21] (there were

no pellets injected at 180° analyzed and were no pellets which have reached the tokamak center). This also confirms the conclusion made in [20,21,22] that the impact of the ∇B-induced drift on the ablation rate of the pellet is rather modest.

However, on ASDEX-Upgrade for the pellets launched at 180° observed was a significant rise of penetration depth (up to about 2.5 times) compared to LFS pellets [7]. Our calculation was performed for the pellet parameters from [7] (r_p = 0.9214 mm, particle content $2\cdot10^{20}$ for both HFS and LFS pellets, $V_p = 130\,\mathrm{m/s}$) and plasma parameters typical for ASDEX-Upgrade but not exactly from the experiment [7] (Figure 10). The calculated penetration depths are $\lambda_p^{(LFS)} \approx 8$ cm and $\lambda_p^{(HFS)} \approx 12$ cm (see Fig. 11), and effect of pre-cooling is rather weak (because evaporation takes place at outer surfaces with high energy content). The difference between measured $\left(\frac{\lambda_p^{(HFS)}}{\lambda_p^{(LFS)}}\right)_{meas} \approx 2.5$ and calculated $\left(\frac{\lambda_p^{(HFS)}}{\lambda_p^{(LFS)}}\right)_{calc} \approx 1.5$ is most probably, besides the inconsistency between experimental and used in simulation ambient plasma profiles, due to the pellet acceleration towards the LFS observed by Müller [12] and Kocsis [23].

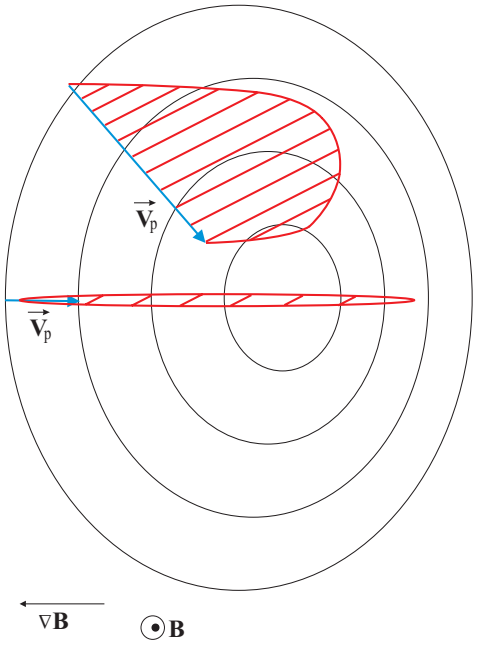

Figure 9. Schematic view of mass deposition areas projected along the magnetic field lines to a certain poloidal cross-section (marked by red shaded areas) for different pellet directions (blue arrows)

The calculated fueling efficiency for LFS pellet (r_p = 1.2 mm, $V_p = 560\,\mathrm{m/s}$, ambient plasma parameters presented in Figure 3) is 12.9%, which coincides well with experimental observation [7] (about 15%), however for HFS pellet it is always 100%, and there is a discrepancy with measured one (about 50%). This discrepancy might be either due to transient increase of radial transport in the presence of steep gradients formed during the pellet injection or due to uncertainty in pellet particle content caused by losses in guiding tube.

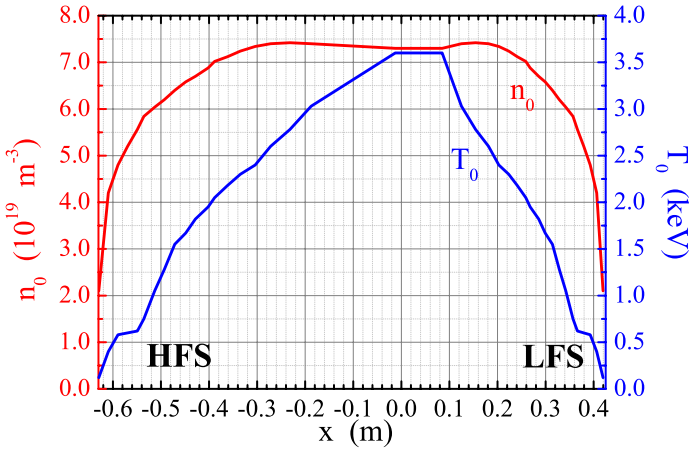

Figure 10. Ambient plasma density and temperature

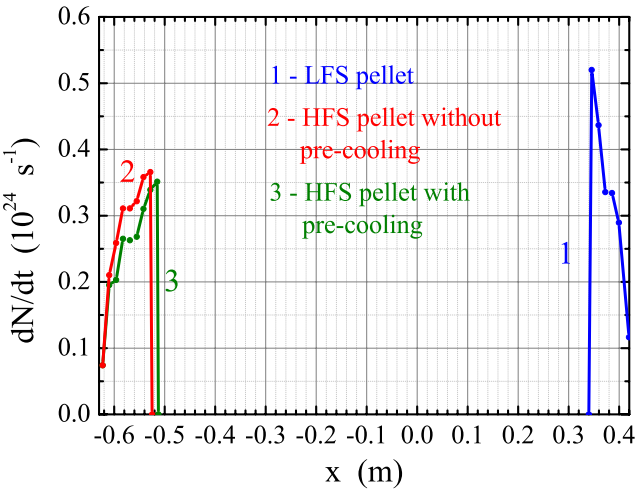

profiles. Figure 11. The calculated ablation rate.

HFS pellet

In Figs. 12 a)-f) the profiles of main cloud parameters are presented for the HFS pellet (r_p = 1.2 mm, $V_p = 560$ m/s, ambient plasma parameters presented in Figure 3). The time 200 μs corresponds to the maximum in the ablation rate. Pellet moves from left to right and is situated at the left boundary of its ablation cloud, because the latter drift in the direction of pellet motion with higher velocity. One can see near the pellet the cigar-shaped dense cold cloud elongated along the magnetic field lines. In Figures 12 a)- c) this 'cigar' is shown in more details, because far from the pellet with $x > -0.25$ m the cloud density n_h is less than $1\cdot10^{22}$ m^{-3}, electrons density n_e and ionization degree are zero. The electrons density, temperature and pressure are plotted up to full radial extension of the cloud. This 'cigar' has the transverse size of about 1 cm and longitudinal size of about $(15 \div 20)$ cm (double side). These values coincide well with the ionization radius l_i and the length equal to $\sqrt{l_i R}$ respectively. It is also seen by the 'wings' on electrons density and temperature plots 12 d) and 12 e) that the particle shift in the pellet wake starts at $z \approx \pm\sqrt{l_i R}$ from the pellet, as it was previously demonstrated in [22]. The results of the simulations show that the size of the neutral cloud formed around the ablating pellet corresponds to the experimentally observed values [12,23] (of the order of several cm) whereas in the previous version of the code without drift (LLP) this value was unreasonably large (see [21,22]). As it may be seen from Figure12 c), the radiating in lines neutral cloud also has a cigar-like shape, which has no 'wings' corresponding to the drift motion. This coincide well with experimental observations of cloud shape, obtained by registering radiation in lines. Thus one can conclude that the new pellet-drift code can qualitatively reproduce the most important characteristics of the pellet cloud.

In Fig. 12 a) arrows show the directions of particle fluxes. Since the neutral particles surrounding the pellet don't drift but move together with the pellet [24,25], a hollow pressure appears just in front of the pellet. Consequently, the particle flux is first directed away from the pellet along the magnetic field (driven by the pressure gradient), then across the magnetic field (due to drift), and then some fraction of the particles are returned back to the cloud axis ($z = 0$).

The cloud temperature (Figure 12 d)) remains less than 2 eV in the vicinity of the pellet, where neutrals exist, and rises rather fast as neutrals burn-out. This occurs because near the pellet the energy deposited in the cloud is spent mainly to ionization and line radiation and only a small part is spent to heating. As neutrals burn out, this energy sink no more exists, and the energy is spent mainly to the heating and expansion. These typical values of density and temperature in the drifting cloud before the pellet (see Figs. 12 c) and d)) qualitatively correspond to those measured by Müller [12] (density of $(1-2)\cdot10^{22}$ m^{-3} and temperature of 20 – 25 eV at distance about several centimeters from pellet).

The drift velocity at different moments is shown in Fig. 13. The velocity rises due to ∇B-induced acceleration, reaches its maximum as the ∇B-induced current vanishes and then comes to zero. Its maximum value coincide well with the estimate [1]

$$V_D^{(\max)} = c_s \sqrt{\frac{\dot{N} m_i}{BRr_\perp}} \sqrt{\frac{\mu_0}{\pi n_0 m_0}}$$

if one substitute $T = 50$ eV into the expression for sound speed. The values of V_D at several centimeters from pellet is about 2×10^4 m/s which is of the order of those measured by Müller [12] 'several thousand meters per second up to $(1-2)\times10^4$ m/s'

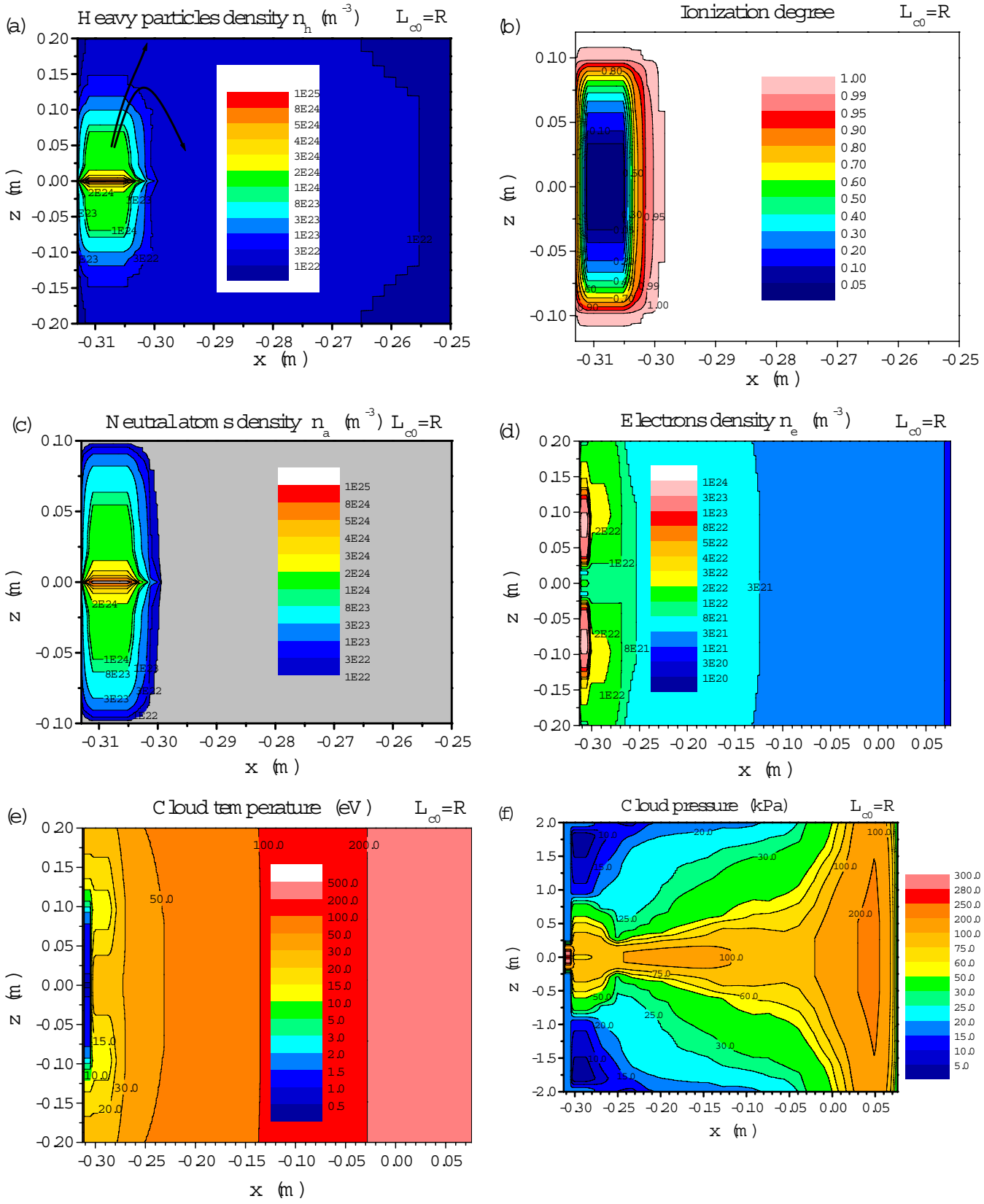

Figure 12. Distributions of main pellet cloud parameters at the moment of the ablation rate maximum for the HFS pellet. The pellet is moving from left to the right and is situated at about $x = -0.3075$ m. Arrows in Figure 12 a) show the directions of particles flow.

The shift distance Δx defined as a distance from the point where particles ablated to the point where they are deposited may be estimated as width of velocity curve in the Fig. 13. In the following Table the shift distance Δx at different moments is presented (Moment t=0 corresponds to a start of pellet ablation). The corresponding pellet position is also shown to make the estimation of the ablation rate value with the help of Fig. 4 easier. Note that the "average" shift distance, calculated according to expression (15a) of [1]

$$\Delta x = \sqrt{\frac{m_i \dot{N}}{B}} \cdot \sqrt[4]{\frac{\mu_0 R c_s}{4\pi D n_0 m_0}}$$

gives $\Delta x = 42$ cm. Here substituted are $D = 1$ m^2/s as the anomalous diffusion coefficient and $\dot{N} = 1.25 \cdot 10^{24}$ s^{-1} as the "average" ablation rate, defined as total number of particles in the pellet over pellet lifetime.

time, μs	Pellet position, m	Δx, cm
200	-0.30	37
250	-0.29	34
300	-0.25	41
335	-0.23	39
370	-0.22	39

LFS pellet

The results of LFS pellet modeling (r_p = 1.2 mm, $V_p = 560$ m/s, ambient plasma parameters exactly ones that are presented in Figure 3) were reported in [10]. The main cloud parameters profiles were similar to those presented in Figs 12, i.e. the neutral cloud had a cigar-like shape, the hollow pressure appeared behind the pellet, the temperature in the pellet wake was about 10 – 20 eV. Only the fueling efficiency differs significantly – for the LFS pellet its value is 13% in agreement with measurements on ASDEX-Upgrade [7].

Thus simulation results demonstrate that the ∇B induced drift strongly affects the process of the pellet cloud motion and the mass deposition after the pellet injection.

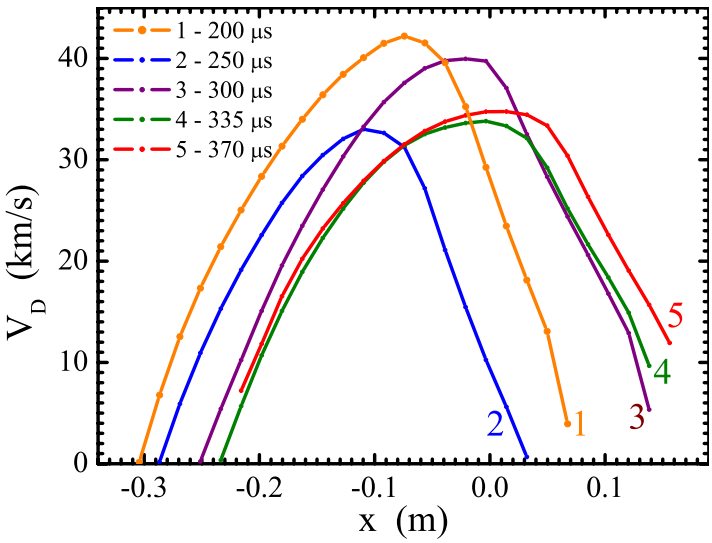

Figure 13. Drift velocity at different moments. Moment t=0 corresponds to a start of pellet ablation.

Conclusions

The new code (LLPD) is developed to model the pellet ablation cloud pattern including the $\vec{E} \times \vec{B}$ drift. Numerical simulation of the pellet ablation and the ablated material redistribution is performed by

means of the new code for HFS and LFS pellets with pellet and plasma parameters typical for ASDEX-Upgrade tokamak. The effect of pre-cooling is studied. Calculation results have confirmed the earlier prediction that the ∇B induced drift strongly affects the cloud parameters (such as density and temperature) and mass deposition profile. The impact of ∇B-induced drift and pre-cooling on the ablation rate is found to be rather modest, at least for pellets which penetration depth is smaller than tokamak minor radius. It is demonstrated that the code can reproduce with acceptable accuracy the ablation rate profile and the penetration depth. It is shown that the pellet cloud structure obtained in the simulation is in reasonable agreement with that reported in the experiments on pellet ablation scenarios in the ASDEX-Upgrade. The fueling efficiency computed on the base of the numerical results is in the same range as in the experiments on ADSEX-Upgrade for LFS pellets, while for the HFS pellets it is always unity.

Acknowledgements

This work was supported by Russian Ministry of Education (grants number A03-2.9-198 and E02-3.2-300).

References

[1] V. Rozhansky et. al. PPCF **46** (2004) 575-591
[2] P.B. Parks et al., Phys. Plasmas **7**, 1968 (2000).
[3] P.B. Parks and L.R. Baylor., Phys. Rev. Letters **94** 125002 (2005)
[4] L.R. Baylor et al., Phys. Plasmas 7, 1878 (2000).
[5] V.Rozhansky, I. Veselova, and S. Voskoboynikov, Plasma Phys. Control. Fusion **37**, 399 (1995).
[6] B. Pégourié and L. Garzotti, in Proceedings of 24th EPS Conference on Controlled Fusion and Plasma Physics 1997, Berchtesgaden, Germany. Europhysics Conference Abstracts Vol. 21A Part I, p. 153.
[7] P.T. Lang et al, Phys. Rev. Letters **79** (1997) 1487
[8] T.T.C. Jones et al., in Proceedings of the 27th European Physical Society Conference on Controlled Fusion and Plasma Physics 2000, Budapest, Europhysics Conference Abstracts Vol. 24B, (European Physical Society), p.13.
[9] J. de Kloe, E. Noordermeer, N.J. Lopes Cardozo, and A.A.M. Oomens, Phys. Rev. Letters **87**, 2685 (1999).
[10] I. Yu. Senichenkov et al, Journal of Nuclear Materials, **337-339** (2005) 446
[11] Lengyel, L.L., et al., Nucl. Fusion **39** (1999) 791
[12] Müller, H.W. et al, Nucl. Fusion **42** (2002) 301
[13] NRL Plasma Formulary, Naval Research Laboratory, Washington, DC. See also Plasma Formulary Web Site http://wwwppd.nrl.navy.mil/nrlformulary/index.html
[14] K.L. Bell et al., J. Phys. Chem. Ref. Data, **12**, (1983) 891.
[15] Lengyel L.L., Rozhanskij V.A., Veselova I.Yu., Nucl. Fusion **36** (1996) 1679.
[16] W.A. Houlberg, et al, Nucl. Fusion **28** (1988) 595.
[17] Lengyel L.L. and Spathis P.N. Nucl. Fusion. **34** (1994) 675.
[18] M. Kaufmann et al., Nucl. Fusion **26**, 171 (1986).
[19] L.L. Lengyel, Nucl. Fusion **29**, 37 (1989).
[20] L. Garzotti, et. al. Nucl. Fusion **37** (1997) 1167
[21] I.Yu. Veselova et al. Proc. of 28th EPS Conference on Control. Fusion and Plasma Physics, Madeira, 2001, ECA, **25A**, 701 – 704

[22] I.Yu. Senichenkov et. al. Proceedings of the 29th EPS Conference on Plasma Physics and Controlled Fusion, Montreaux, 2002, ECA **26B** P-4.081
[23] G. Kocsis, S. Kalvin, G. Veres, Review of Scientific Instruments **75** (2004) 4754
[24] I.Yu. Veselova, V. Rozhanskij. Sov. J. Plasma Phys. 17 (1991) 817
[25] P. Parks. Nucl. Fusion 32 (1992) 2137.
[26] P.T.Lang et al., Nucl. Fusion **41** (2001) 1107.